Journal of Materials Chemistry A

Understanding the Mn Dissolution Mechanism in Rock Salt-Type $Li_4Mn_2O_5$ Cathodes

Journal:	*Journal of Materials Chemistry A*
Manuscript ID	TA-ART-03-2025-002560.R1
Article Type:	Paper
Date Submitted by the Author:	12-May-2025
Complete List of Authors:	Theibault, Monica; Lawrence Berkeley Laboratory, Nordlund, Dennis; Stanford Synchrotron Radiation Lightsource, Dun, Chaochao; Lawrence Berkeley National Laboratory, Urban, Jeffrey; Lawrence Berkeley National Laboratory, Tong, Wei; Lawrence Berkeley National Laboratory, Energy Storage and Distributed Resources Doeff, Marca; Lawrence Berkeley National Laboratory,

Understanding the Mn Dissolution Mechanism in Rock Salt-Type $Li_4Mn_2O_5$ Cathodes

Monica Theibault,[a] Dennis Nordlund,[b] Chaochao Dun,[c] Jeffrey Urban,[c] Wei Tong,*[a] and Marca Doeff*[a]

*corresponding authors

[a]Energy Storage and Distributed Resources Division, Lawrence Berkeley National Laboratory Berkeley, CA 94720, USA.

[b]Stanford Synchrotron Radiation Lightsource, SLAC National Accelerator Laboratory, Menlo Park, CA 94025, USA

[c]The Molecular Foundry, Lawrence Berkeley National Laboratory, Berkeley, CA 94720, USA.

Abstract

Herein, we apply a suite of synchrotron and lab scale X-ray techniques to both the cathode and the separator harvested from pristine, charged, or cycled lithium half-cells containing the disordered rock salt (DRX) material $Li_4Mn_2O_5$, in order to understand Mn dissolution processes throughout charging and discharging. Previous research has hypothesized two concurrent effects that may drive Mn dissolution in cells during cycling: acid-induced disproportionation of Jahn-Teller active Mn^{3+} and structural rearrangement of the cathode lattice. Through depth probing of the Mn oxidation state in both the cathode and separator via soft X-ray absorption spectroscopy (XAS), hard XAS, and X-ray photoelectron spectroscopy (XPS) at progressive states of charge, as well as extended X-ray absorption fine structure (EXAFS) analysis of the local Mn environment, the primary driving force of Mn dissolution is determined to be high-voltage structural rearrangement above 4.2 V. Mn dissolution is, additionally, a main source of capacity fade in $Li_4Mn_2O_5$ DRX cells, which retain only 59% capacity after 20 cycles.

Introduction

To meet the ever-increasing demand for power, the search for new cathode materials with improved performance and lower cost has led to the development of Li-excess disordered rock salts (DRX). In DRX materials, Li is randomly intermixed with one or more transition metals on octahedral sites of the crystal lattice. Some DRX materials are capable of achieving capacities that are higher than traditional layered cathode materials.[1–5] Additionally, the DRX structure can accommodate a wide range of metals and relieves dependance on Ni and Co currently used in layered cathodes.[6] The best performing DRX materials contain excess Li, utilize Mn redox, make use of fluorination to suppress oxygen loss, and may contain other earth-abundant metals like Ti.[4,5,7,8] However, manganese dissolution is a major challenge that limits cycle life in many Mn-based cathode materials, including spinel and Li, Mn-rich (LMR) layered oxides.[9]

The exact mechanism of Mn dissolution is still not entirely understood even though the study of this phenomenon predates the use of lithium manganese oxide spinels as cathodes in lithium-ion batteries. In 1981, experiments revealed that acid treatment converts $LiMn_2O_4$ to λ-phase MnO_2, which preserves the spinel crystal structure while removing lithium ions.[10] In the 1990s, extensive research was conducted on spinel cathodes, which offered better thermal stability, and thus improved safety, compared to other transition metal oxides.[11,12] A distinct drawback, however, was that full cells with spinel manganese oxide cathodes underwent steep capacity decay, particularly when temperatures were raised to 55^{o} C or above.[13,14] While modifications such as compositional variations, partial substitutions, and fluorination[15–18] have ameliorated Mn dissolution to some extent, solutions to the problem remains elusive. Even with state-of-the-art electrolyte solutions, cells containing manganese oxide spinels exhibit shorter cycle life than commercial alternatives such as layered lithium nickel manganese cobalt oxide (NMC) cathodes. A similar issue is found for other electrode materials in which Mn is redox active such as lithium and manganese-rich layered oxides (LMRs).[19–21] This is in contrast to conventional NMCs, wherein only Co and Ni undergo redox processes, and have much higher cycle life.[22,23]

Extensive efforts have been made to explore the diverse composition space (transition metals and what their unique electrochemistry adds to DRX redox behavior) and bulk phenomena (structural evolution and cathode/electrolyte decomposition) for this relatively new family of DRX materials to address issues such as limited cycle life and voltage decay. However, research on Mn dissolution in DRX materials has been limited, and further work is necessary to determine to what degree this dissolution occurs and under what circumstances. Changes to the surfaces and interfaces during cycling can provide insights into the processes of Mn dissolution at various states-of-charge. Concomitant oxidation/reduction processes and structural changes occur during charging and discharging, and therefore the key to understanding Mn dissolution mechanism involves decoupling the impacts of each. The utilization of the Mn^{3+} /Mn^{4+} redox couple in DRX cathodes pre-dispose these materials to disproportionation to Mn^{2+} and Mn^{4+} in the presence of adventitious water or protonated electrolyte decomposition products, as are commonly found in cell environments.[24,25]

In 2016, Pralong et al. reported a material with the nominal composition $Li_4Mn_2O_5$ (LMO) having an ultrahigh discharge capacity of 355 mAh/g, but with severe capacity fade.[3] Incorporation of $LiMn_2O_4$ spinel during synthesis improved cycling stability while retaining a reversible discharge capacity of 250 mAh/g.[26] (Note that the delivered discharge capacity varies with current density and voltage limits for both the original and spinel-modified materials). The original LMO material undergoes significant Mn dissolution at room temperature, as evidenced by discoloration of the lithium anode after just one cycle at room temperature.[26] The simplicity of the composition and close structural relationship to other DRX materials make LMO an ideal subject for the study of Mn dissolution. The high Mn content and electrolyte-flooded coin cell environment exacerbate the dissolution effect,[27] making dissolved Mn readily detectable in both lab and synchrotron experiments. Here, we used advanced X-ray techniques such as X-ray absorption spectroscopy (XAS) and X-ray photoelectron spectroscopy (XPS) to track Mn dissolution in coin cells containing LMO. We find that some Mn dissolution occurs even when pristine electrodes are soaked in electrolyte for a few days, but dissolution accelerates after cells are charged past 4.2 V, consistent

with the observed performance degradation. The resultant signal of the Mn on the separator via these techniques is distinct from the cathode signal, suggesting that the dissolved Mn undergoes further reactions during charging and discharging. Combining electrochemical and X-ray analysis, we propose that structural rearrangement upon cycling is a significant contributing factor to Mn dissolution in LMO cathodes.

Experimental

LMO Synthesis and Characterization

Precursor materials Mn_2O_3 (Sigma Aldrich, 99.9%) and Li_2O (Sigma Aldrich, 100 mesh, 99.5%) were added in stoichiometric amounts to an air-tight ball mill jar in an argon-filled glovebox with H_2O and O_2 levels less than one ppm and milled in a Retsch PM200 per previous literature instructions with slight modifications.[3,26] They were milled for one hour at 600 rpm, then allowed to rest for 30 minutes, repeated in an automatic program sequence for a total milling time of 24 hours. X-ray diffraction (XRD) patterns were obtained on the as-made materials using a BRUKER D2 powder X-ray diffractometer equipped with a Cu Kα radiation source (λKα1 = 1.5406 Å, λKα2 = 1.54439 Å, 40 kV, 30 mA). Scanning electron microscopy/energy dispersive X-ray spectroscopy (SEM/EDS) was performed at 15 kV using a Zeiss Ultra-55 Field Emission Scanning Electron Microscope (FESEM) coupled to a Bruker X-Ray EDS detector.

Cell Construction

The synthesized LMO material was milled with Super P Carbon (Timcal) for an hour at 600 rpm in a ratio of 7:2 LMO:Super P. This mixture was then milled by hand with poly(vinylidene fluoride) (PVDF) and N-methyl-2-pyrrolidone (NMP) in a mortar and pestle for a final ratio of 7:2:1 LMO:Super P:PVDF. The mixture was then cast onto a carbon coated aluminum current collector to form the cathode and dried in a vacuum oven for 12 hours at 120° C. Coin cells were assembled with a ½ inch diameter cathode (approximate mass loadings of 1.0-1.5 mg/cm^2), a 1 mm thick Whatman GF/F separator, a 5/8-inch diameter lithium metal anode, and 130 uL of an electrolytic solution of $LiPF_6$ in 1:1 EC/DEC.

Cell Cycling

Electrochemical cycling was performed on a Biologic VMP-3 multichannel cycler at a C-rate of 0.05 where 1C is defined as 247 mAh/g. Current was applied to cutoff voltages of 4.8, 4.6, and 4.2 V, and then cells were discharged to 2.0 V. All cell cycling was performed at room temperature.

X-Ray Techniques

All cathode and separator samples taken from deconstructed cells were washed with DMC and dried in an argon-filled glovebox. Ex situ Mn K-edge hard X-ray absorption spectra (XAS) were collected in fluorescence mode using a Si (220) monochromator at beamline 4-3 at Stanford Synchrotron Radiation Lightsource (SSRL). X-ray absorption near edge structure (XANES) data analysis was performed using multiple methods, outlined in detail in previous papers.[28] EXAFS analysis was performed using Athena and Artemis via IFEFFIT's programming interface. Ex situ Mn L-edge and O K-edge soft XAS spectra were collected at beamline 8-2 at SSRL under ultrahigh vacuum (10^{-9} Torr) at room temperature using the total electron yield (TEY) and fluorescence yield (FY) detection. X-ray photoelectron spectroscopy (XPS) experiments were performed at the Molecular Foundry with a Thermo-Fisher K-Alpha Plus XPS/UPS (Al Kα source λ = 1487 eV) and all spectra were calibrated to a C 1s signal of 284.8 eV. Certain experiments were performed in duplicate as indicated in the text.

Results and Discussion

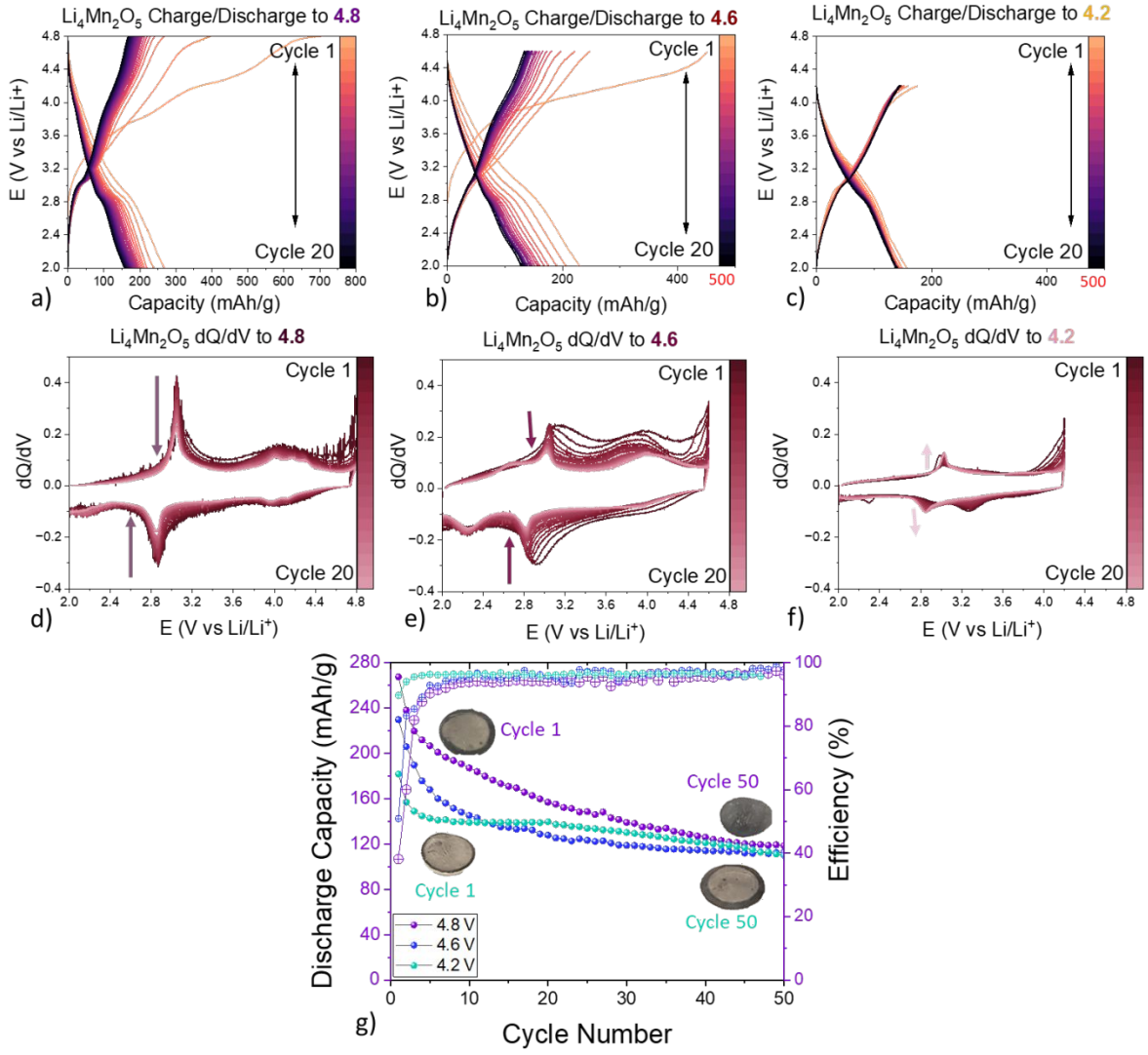

Figure 1. a,b,c) Charging/discharging curves of LMO half-cells cycled between 4.8 V and 2.0 V, 4.6 V and 2.0 V, and 4.2 V and 2.0 V respectively. d,e,f) dQ/dV plots of cells cycled between 4.8 V and 2.0 V, 4.6 V and 2.0 V, and 4.2 V and 2.0 V respectively. Arrows indicate decreasing Mn redox peak height (e,f) or increasing Mn redox peak height (f). g) Capacity retention of cells cycled to 4.8 V (purple), 4.6 V (blue), and 4.2 V (aqua) with images of the lithium anode at each potential, showing discoloration (inset).

LMO was synthesized by a reactive ball-milling method. The XRD pattern shows broad peaks consistent with a nanocomposite rock salt structure and is shown in Figure S1. LMO half-cells were cycled between 4.8, 4.6, or 4.2 V and 2.0 V. As previously reported for this material,[3,26] the initial charging cycle

has a very high initial capacity, with the exact value dependent upon the charge limit used. For the cell charged to 4.8 V, there are multiple plateaus, suggestive of side reactions occurring with the electrolyte, as well as electrochemical decomposition of Li_2O or Li_2CO_3, present in the as-made material. The discharging curve only has one plateau at 2.90 V. The first-cycle discharge capacities of LMO cells are dependent on the conditions used and details of the synthesis, sometimes exceeding 350 mAh/g.[3] For the cell charged to 4.8 V, the initial discharge capacity was significantly lower at 268 mAh/g. The capacity decreased severely over 50 cycles to 119 mAh/g. Capacity fading during cycling is, however, less severe for cells charged repeatedly at lower voltages. While the cell charged to 4.2 V has a lower initial discharge capacity it demonstrates a better capacity retention of 87% after 20 cycles, versus 59% for the 4.8 V cell. The initial capacity advantage of the 4.8 V cell is nearly erased by the 50^{th} cycle. For all the cells, first-cycle coulombic efficiencies (Figure 1g) were significantly lower than for subsequent cycles, primarily due to side reactions such as oxygen loss that occur mostly on the first cycle. In addition, initial coulombic efficiencies are higher for cells charged to lower potentials than for those charged to 4.8V.

Differential capacity (dQ/dV) plots for the cycled cells give indications of processes taking place during charge and discharge. The first charge cycle shows a large charging peak at approximately 3.05 V and an associated discharging peak at approximately 2.87 V, attributed to the Mn^{3+}/Mn^{4+} redox couple.[3] Upon cycling 20x, the peak shifts to lower potentials for the cells cycled between 4.8 V and 2.0 V, as well as those cycled between 4.6 V and 2.0 V (Figure 1d,e), due to increased cell impedance and structural changes upon cycling. The peak intensity is also reduced from cycle 1 to cycle 20, reflecting the loss of capacity. For the cell charged to 4.8 V, we also observe a more diffuse set of peaks appearing at approximately 4.0 V, suggestive of structural change to a spinel-like phase.[26] The 4.6 V cell also shows an increasing peak at approximately 2.25 V absent in the 4.8 V or 4.2 V cell. Interestingly, in contrast to higher-voltage cells, the Mn redox peak for the 4.2V cell increases in intensity upon cycling (Figure 1f).

Discoloration of the lithium anodes is evident in some of the half-cells upon post-mortem analysis (insets, Figure 1g), particularly in those charged above 4.2 V. The discoloration is particularly strong in the

region *surrounding* the lithium/ separator /cathode interface. The ½ inch diameter cathode is smaller than the 5/8-inch lithium anode, and the greatest discoloration happens in the areas where there is lithium not directly facing the cathode. After cell cycling 50x between 4.8 V and 2.0 V, the entire lithium anode was completely discolored whereas in cells charged between 4.2 V and 2.0 V, only the region surrounding the lithium/ separator /cathode interface was discolored. This suggests that deposition of Mn on the lithium anode is likely one reason for the capacity fade in the cells cycled to 4.8 V. This Mn deposition, brought about by Mn dissolution from the active material, occurs along with structure change as well as oxygen release and electrolyte oxidation.[26] These phenomena occur to a much lesser extent in the cells cycled to 4.2 V.

Post-cycling SEM images show changes in the morphologies of the electrodes. The pristine LMO powder and material in the pristine cathode pre-cycling show distinct particles of LMO (Figure S2). However, after 50 cycles, the particles are less distinct and appear to be covered by a surface film. EDS elemental mapping at the surface level shows distinct areas with less Mn in the cycled electrodes compared to the pristine one, particularly after 50 cycles, consistent with the formation of a surface film upon cycling which contains less Mn than the original active material.

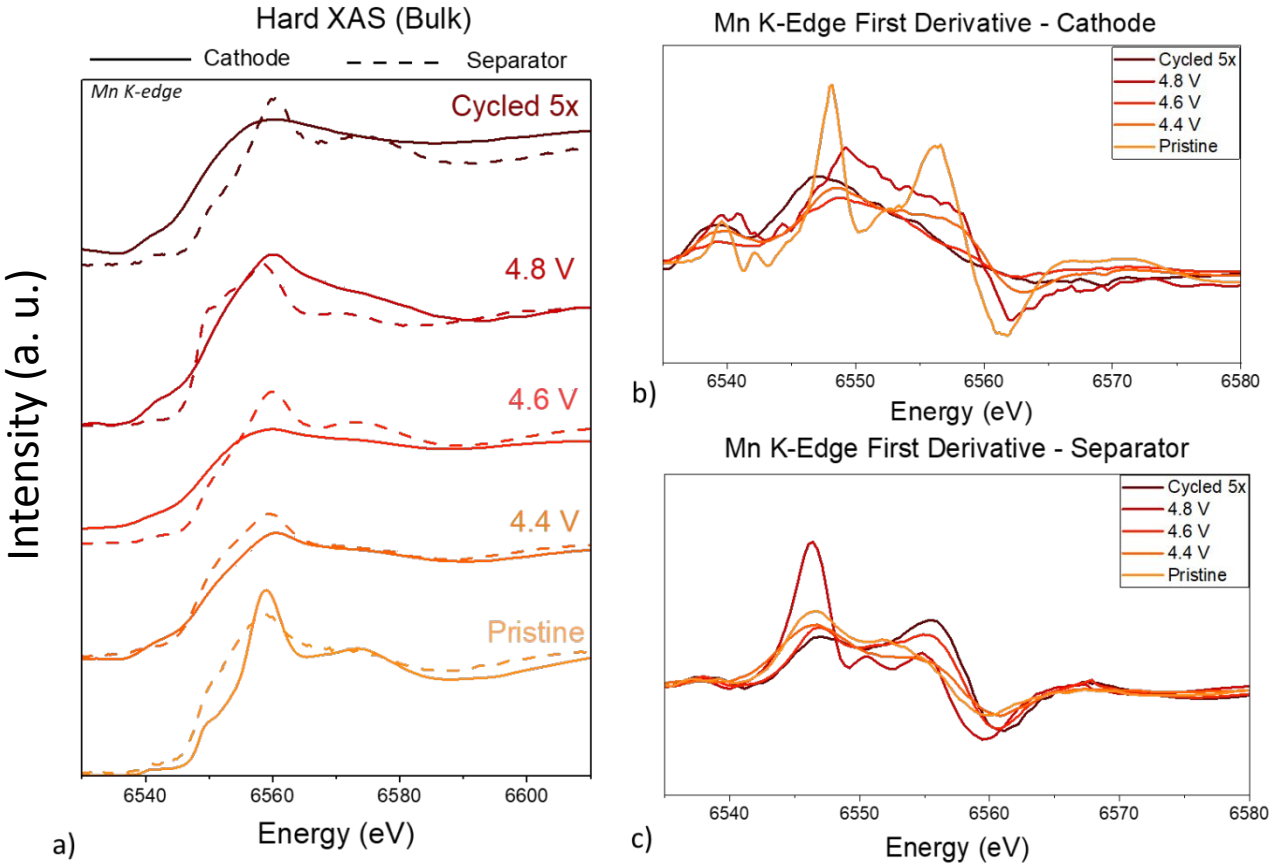

Figure 2. a) *Ex-situ* Mn K-edge XAS of LMO cathodes and separators taken from cells charged to 4.4 V, 4.6 V, or 4.8 V. The pristine separator was taken from an assembled but uncycled cell that was left to rest at room temperature for 7 days before data collection. The pristine cathode was not exposed to electrolytic solution prior to measurement. All other cells were disassembled within 12 hours of cycle completion. b) First derivative of *ex-situ* Mn K-edge of LMO cathodes. c) First derivative of *ex-situ* Mn K-edge of LMO separators.

In Figure 2, Mn K-edge XAS data was collected for both separators and cathodes harvested from LMO cells charged to 4.4 V, 4.6 V, or 4.8 V, with measurements penetrating into the bulk. The pristine LMO spectrum displays a peak absorption edge at 6558.7eV that closely matches that of Mn K-edge from

Mn_2O_3, indicating a 3+ oxidation state. We observe noticeable spectral differences for the different charging voltages but with relative broad features.

There are multiple methods used for peak position analysis of Mn K-edge XANES spectra since detailed linear combination analysis is complicated when the local structure such as symmetry, bond length and angles are modified.[28,29] When limiting the valence state analysis to an approximate oxidation state extracted via the onset of the edge, different formal oxidation states (2+,3+,4+) are found to be linearly related to the oxidation state.[29] Here we apply the first derivative method to qualitatively evaluate the Mn valence at specific points during the charging/discharging process (Figure 3b/c and Figure S3a, and reference standards in Figure S4). For alternative methods to evaluate the edge onset see Figure S3b,c and the discussion in Supp. Mat of Ref Nam.[28]

For the LMO cathode, the pristine material has a first derivative peak at approximately the same location as the first derivative peak of Mn_2O_3 (6548.0 eV), indicating trivalent Mn. This was confirmed by soft XAS measurements, which will be discussed in detail later. As the cell was charged to 4.4 V, the peak energy of the first derivative increased slightly to 6548.5 eV, a trend that continues throughout the charging process (6549.2 eV at 4.8 V), consistent with increased Mn oxidation. For the electrode cycled 5 times ending in a discharge step, the first derivative peak energy was found at 6546.8 eV which suggests a more reduced state compared to the pristine cathode (also affected by changes in bond lengths and coordination due to structural rearrangement as confirmed by EXAFS, see discussion below).

Hard XAS measurements on the separator revealed a dynamic Mn dissolution process. When an uncycled cell was rested for 7 days, the separator showed Mn peak location at the same energy as the Mn in the cathode, though the spectral shape is slightly different. However, for the separators in the cells that were cycled under typical conditions, Mn appeared to be in the trivalent state as well. This suggests that Mn^{2+} undergoes further electrochemical reactions after dissolving and deposits on the separator in the trivalent state. This will be further investigated as we deploy surface sensitive X-ray techniques to provide additional insight into the Mn dissolution dynamics.

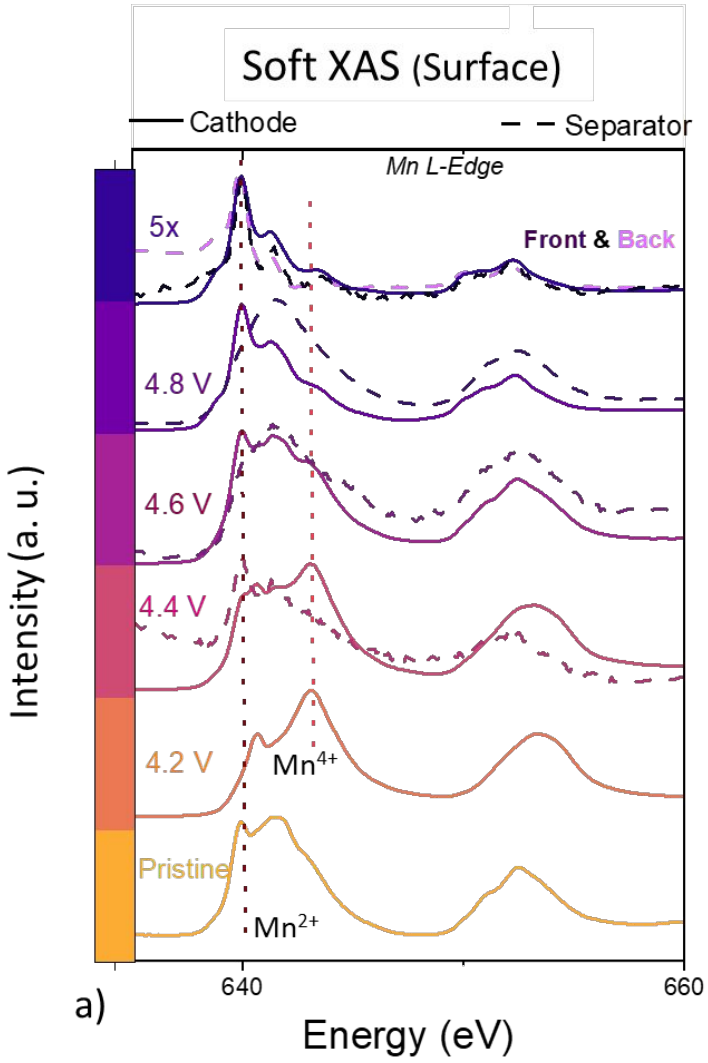

Figure 3. Total Electron Yield (TEY) Mn L-edge XAS taken of the cathode and separator removed from cells at indicated points during charge, or after cycling between 4.8 V and 2.0 V five times, stopped in the discharged state. Straight dashed lines are guides for the eye representing the location of the peaks of reference MnO (Mn^{2+}) and MnO_2 (Mn^{4+}). "Front" and "back" refer to the side of the separator facing the cathode and the anode, respectively.

To gain detailed insight into the chemical state of surface Mn on both the cathode and the separator, we performed Soft XAS (Mn L-edge) and XPS before and after cell cycling (no long pre-soaking). Mn L-

edge XAS is a more sensitive probe of Mn valence as it probes TM3d transitions directly via 2p-3d dipole excitation. Furthermore, while hard XAS measures the electronic structure of Mn in the bulk (depth of a few μm), soft XAS measures about 5 nm into the surface in total electron yield (TEY) mode and 50-100 nm into the bulk in fluorescence yield (FY) mode.

Figure 3 shows the Total Electron Yield (TEY) Mn L-edge XAS acquired from the cathode and separator removed from cells charged to 4.2 V, 4.4 V, 4.6 V and 4.8 V, as well as after 4.8 V - 2.0 V cycling five times and stopped in the discharged state. Reference soft XAS spectra of MnO, Mn_2O_3, and MnO_2 were taken for comparison and are shown in Figure S5. The Mn L-edge XAS results for the pristine LMO electrode (with no soaking procedure) are similar to that of Mn_2O_3, but there is a low energy shoulder appearing close to the one found for MnO, indicating that the surface is slightly reduced (A linear combination analysis gives an average oxidation state of +2.8). At 4.2 V, the Mn L-edge spectrum of the cathode is shifted to higher energy consistent with oxidation to the tetravalent state but this trend is reversed at higher potentials, indicating reduction of Mn near the surface. After charging to 4.8V, the surface Mn is primarily in the 2+ oxidation state. Oxygen loss from the surfaces of LMO electrodes has been observed on the first charge in differential electrochemical mass spectroscopy experiments,[26] which would result in reduction of Mn at the surface. Subsequent dissolution and/or reactions with electrolytic solution may also alter surface Mn oxidation states. A comparison between the TEY and FY mode (Figure S6) indicates that changes in Mn oxidation is not limited to the very outer-most surface region but penetrates ~100 nm into the material.

The spectra from separators removed from the charged cells are displayed as dashed lines in Figure 3. Note that the spectra have been renormalized to allow for comparison and the absolute signal is much weaker than on the cathode side (too weak for meaningful FY spectra). The Mn signal was below the detection limit for the separator taken from the 4.2 V charged cell (note that this cell was not subjected to a long soaking period). At 4.4 V, a small signal was observed, showing a reduced state compared to the cathode. After cell charging to 4.6 V and 4.8 V, the separator shows higher Mn oxidation state compared

to that on the surface of the cathode, whereas after 5 cycles, ending on a discharge (2.0 V), Mn in both the cathode and the separator is in a primary 2+ state (Figure 3), indicating ongoing Mn^{2+} dissolution and migration across the electrolyte. For this sample, in addition to the measurement on the side facing the cathode ("front" side), we also measured the side facing the anode ("back" side). This measurement confirmed that there was no significant difference in Mn deposition at the lithium-separator interface relative to the cathode-separator interface.

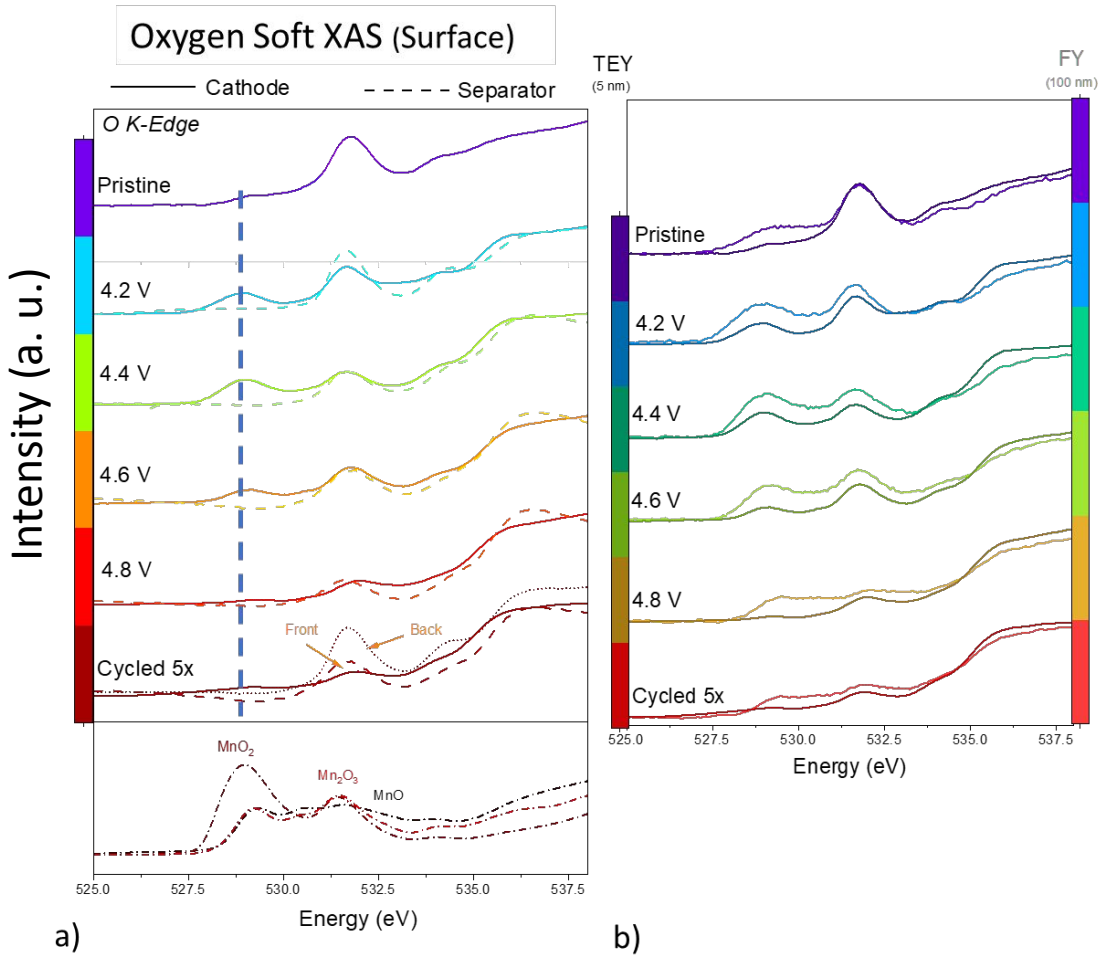

Figure 4. a) O K-edge XAS in TEY mode obtained on the cathode (solid lines) and separator (dashed lines) taken from cells charged to indicated limits or cycled, stopped in the discharged state. The front of the separator faces the cathode and the back faces the anode. The bottom panel shows spectra of reference

materials. The vertical dashed line is provided as a guide to the eye; b) O K-edge XAS obtained on the cathode in FY and TEY modes (~100 nm and 5 nm depths respectively).

Figure 4 shows the O K-edge XAS collected from the same cells as in Figure 3 measured in TEY mode (Figure 4a) and TFY mode (Figure 4b), along with reference compounds displayed in the bottom panel for comparison. The figure is zoomed in the pre-edge region which covers transitions from O1s into hybridized TM3d-O2p states (TM=transition metal).[30] Full analysis of O K-edge energies for LMO cathodes has been described in previous papers.[26] The O K-edge XAS spectra of octahedrally coordinated transition metal-oxygen bonds in manganese oxides will feature 2 states below 532eV associated with the t_{2g} and e_g states of the octahedral symmetry along with a broader 4sp broad band above 535eV.[30] This region also covers π^* states for some stable oxygen-containing organic by-products such as carbonyl (~532eV) and carbonate (~533eV).

A comparison between the FY and TEY spectra for the cathodes (Figure 4b) shows that the near-surface as probed by TEY has a significant contribution of oxygen-containing organic species (carbonyl). Fractional contributions of carbonyl species increase the signal around 532eV which merges with the e_g peak, adding intensity and a slight shift to higher energies. With respect to the chemical state of Mn, the O K-edge dataset corroborates the findings in the Mn L-edge data. We first observe the trend in the FY spectra, which has less interfering contribution from oxygen-containing organic compounds, and find an initial oxidation towards a tetravalent state when charged to 4.2 V, followed by a Mn reduction as a function of voltage, similar to the Mn L-edge data. The 4.8 V charged cathode as well as the cathode cycled 50x display a spectrum that closely resembles the O K-edge from hexagonal Mn^{2+}, which is also observed in the Mn L-edge data.

Comparing the near-surface (top ~5nm) TEY spectra versus the FY (top ~100nm), we can deduce some further trends in the buildup and dynamics of the topmost layer of surface organic compounds with respect to oxygen species. Interestingly, the pristine cathode has a rather strong carbonyl contribution as well as some carbonate which penetrates deeper than the TEY probe (beyond a few nm), and is attributed

to surface organic compounds. Upon charging, TEY and FY show a relatively weaker organic contribution (relative to its Mn-O states), yet with some significant organic presence both in the top few nm but also a bit further into the cathode. At 4.8 V and for the sample cycled 5x, the FY closely resembles that of Mn^{2+} without significant organic contribution, while at the same time having a top layer with a strong contribution from oxygen containing organic compounds, indicating the presence of a Mn^{2+} dominated near-surface layer and the formation of a more stable top-surface reaction layer composed of organic compounds.

The signal from the separators (dashed, Figure 4a) is shown in TEY mode and compared with the corresponding cathode spectra. (The signal to background was rather weak, and the FY signal was not strong enough to give meaningful data for comparison). In all the separator samples, we find that the spectrum is dominated by a peak near 532 eV associated with carbonyl groups. It should be noted that the separator used is glass fiber, which contains SiO_2, but that SiO_2 has no features below 537 eV,[30] and thus its contribution in this region can be ruled out. A feature near 534 eV can be observed in the spectrum acquired from the back of the separator (side facing the anode) recovered from a cell cycled 5 times and also to a smaller degree from the front. This can be assigned to Li_2CO_3, which may come about from decomposition of carbonate solvents. We note that there is some contribution at 534 eV also in the pristine sample and in the 4.2 V separator, and we assume that the separator when soaked (no data for this sample) will have some carbonate contribution before the initial charge.

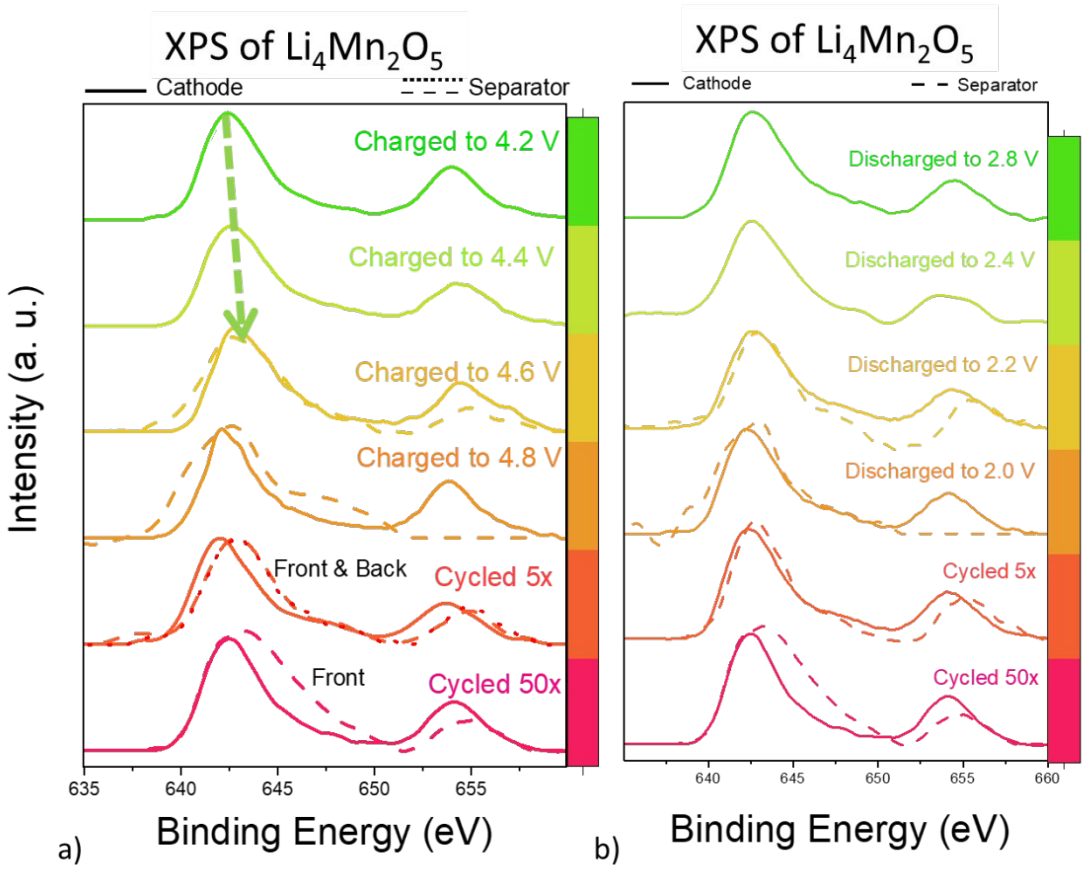

Figure 5. Mn XPS of LMO cathodes and separators taken from cells at indicated points during the (a) charging and (b) discharging process. Data on both plots for components extracted from cells cycled between 4.8 V and 2.0 V five or fifty times, stopped in the discharged state, are also shown. The labels "front" and "back" refer to the side of the separator facing the cathode and the anode, respectively.

XPS, which probes the outermost surface (depth of ~1-2 nm) of the components, corroborates some of the trends shown via soft XAS (Figure 5). First, we focus on the changes upon charging (Figure 5a) which was recorded from similar sample conditions to the previously discussed hard XAS (Figure 3) and soft XAS (Figure 4) results. There was no signal from Mn in the XPS of the pristine cathode, although Li and O were detected, suggesting that electrolyte related products such as lithium carbonate covers the surface and blocks the Mn signal. The $Mn2p_{3/2}$ peak in XPS for the cathode charged to 4.2 V was found at a binding energy of 642.4 eV, just below the expected location of Mn in MnO_2 (642.5 eV), similar to the

oxidation state observed in soft XAS.[31] Upon further charging, the $Mn2p_{3/2}$ peak is slightly shifted to 642.6 eV (4.4V) and 642.7 eV (4.6V), indicating fractionally more oxidized Mn. At 4.8V and for the cells cycled 5x, we observe a significant downward shift to 642.1 eV (4.8 V) and 642.0 eV (5x cycled), consistent with a surface Mn reduction. Depth profile measurements of the cell charged to 4.4 V and the cell cycled 50x (Figure S7) indicate a slight trend (0.1-0.2 eV shift) towards lower oxidation states with increasing etch time. Although XPS follows the same overall trend as observed in the Mn L-edge data, we note that XPS indicates that at the outermost surface, there is prevalence of some fraction of Mn with higher oxidation state.

At the outermost (~1 nm) surface of the separator, we find that $Mn2p_{3/2}$ remains at approximately the same oxidation state in the cells charged to 4.6 V and to 4.8 V (642.58 eV and 642.61 eV, respectively), consistent with the soft XAS (~5nm) that showed a valence state of +3.2 at both potentials. For the cells cycled 5x, however, while soft XAS showed that on average (within the top ~5 nm) Mn at the separator was dominated by species in the +2 state, we find that the $Mn2p_{3/2}$ XPS peak is only 0.3 eV lower than that of the cell charged to 4.2 V, indicating a non-negligible fraction of Mn at higher oxidation state at the very outermost surface. We interpret this as evidence of Mn disproportionation reactions occurring at the surface, which leaves some higher oxidation state Mn present at the outermost surface even if a more reduced Mn is stabilized at higher voltages upon cycling.

O1s XPS can provide important information about the cathode-electrolyte interface during charging and discharging, both for lattice bonded (O-Mn) and oxygen-containing organic species. O 1s XPS (Figure S8a) on charged cathodes shows peaks for the O-TM bond at approximately 529.5 eV, consistent with Mn^{4+}, and then a broad peak between 530 and 535 eV that is an amalgamation of lower energy C=O bonds and higher energy C-O bonds. The pristine cathode appears to primarily have a signal from carbon-oxygen bonds, with C-O bonds dominating, though both C-O and C=O bonds appear, likely from lithium carbonate. At all points during charging, the O1s spectra show a (low energy) Mn-O peak along with oxygen-containing organic species at various ratios. At the end of charge, 4.8 V, the cells show the strongest O-Mn

signal, indicating possible consumption of surface organic compounds, surface rearrangement, or the oxidation of Mn forming new surface Mn-O bonds. Depth profiling (Figure S8b,c) of cathodes charged to 4.4 V as well as cathodes after 50 cycles, at the end of discharge, additionally revealed that the surface is covered by an ultrathin layer of surface organic compounds. Etching of the cathode surface for 120 s and 240 s reveals a progressively stronger O-Mn bond signal as the surface layer is removed. There is also a slight shift of the O-Mn bond towards lower energies (which separates the shoulder further from the main peak) for the 4.4 V charged sample, which is due to the increased presence of higher valence Mn.

Figure S9 shows C1s XPS including depth profiling from the same samples as for O1s. We note that the pristine sample has significant contribution from PVDF components (CF_2 groups at 292 eV and chemically shifted aliphatic carbon at around 286.5 eV) but also contributions at ~291 eV from Li_2CO_3 and many other functionalities (C-C, C-H, C-O, C=O) giving rise to broad features. Upon charging, the spectra show a progressive lowering of C-Fx, C-O and C=O groups, which is stabilized with relatively minor oxygen functionalities with some fraction of carbonate at the end of charge (4.6 V and 4.8 V), before growing stronger again in the cell cycled 50x, at the end of discharge. Depth profiling (Figure S9b) for both analyzed cells (4.4 V and cycled 50x) primarily indicates that any peaks not associated with adventitious carbon (284.8 eV), i.e., carbon-oxygen signals and Li_2CO_3, are at the very top surface, as they are significantly reduced after 120 s and 240 s etching, consistent with the O1s data.

We also recorded the Mn2p XPS spectra throughout the discharging process, shown in Figure 5b. We note that all the discharged samples are centered around 642.4+/-0.1eV, with a slightly less reduced Mn for the sample discharged to 2.8 V. Further cycles (5x and 50x) do not change the spectrum significantly. We also note that the discharged sample is similar to the 4.8 V charged sample, indicating that most changes to Mn at the topmost surface are driven by surface oxygen loss (as outlined by Yin et al.)[26] creating a fraction of oxidized Mn-O species which are eventually reduced upon further charging, and that discharging plays a relatively minor role in Mn oxidation state. Given the small binding energy shift of the $Mn2p_{3/2}$ XPS peak, we conclude that there is a non-negligible fraction of Mn at higher oxidation state

at the very outermost surface, even though the near-surface (~5nm) region shows mostly lattice Mn in the 2+ state, according to soft XAS. The presence of some higher valent Mn at the topmost surface throughout the charging and discharging process, all the while charging at higher voltages, stabilizes Mn^{2+} in the near-surface region, indicating dynamic surface reactions take place resulting in quite significant depth dependence during cycling. To better understand the dynamics of the Mn chemical state in the surface region, key results from all three x-ray methods, hard XAS, soft XAS, and XPS, are summarized in Figure 6 and discussed in the following.

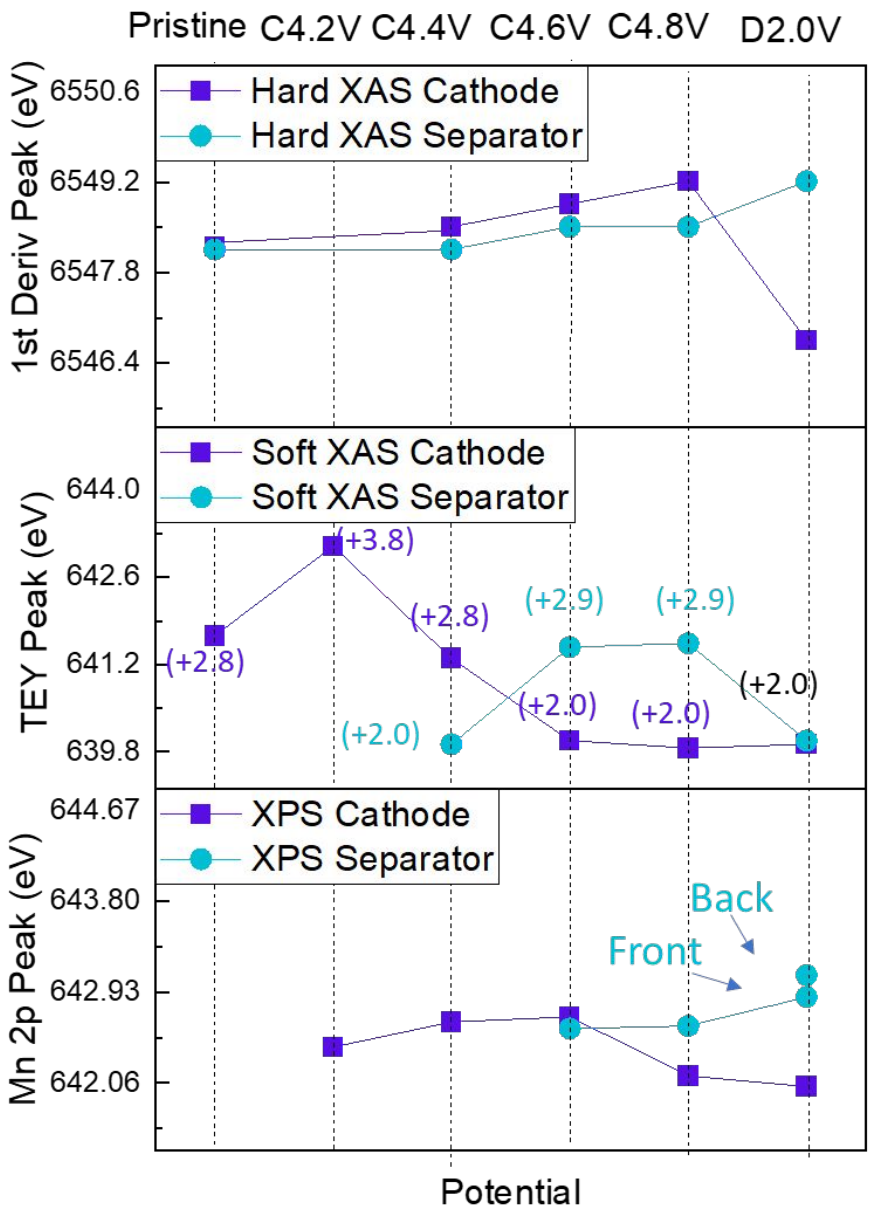

Figure 6. Changes in energies of Mn signals for (from top to bottom) hard XAS, soft XAS in TEY mode (5 nm depth), and XPS from cathode and separator taken from cells at various states of charge and discharge. Soft XAS measurements indicate the oxidation state of the cathode at various states of charge, determined from reference spectra (Figure S5). D2.0V indicates that the cathode was cycled 5x, ended in the discharge state at 2.0 V.

The different trends in Mn oxidation state, K-edge, and L-edge gained from the different X-ray techniques paint a dynamic picture of Mn dissolution in the cell (Figure 6). XPS measures the very surface (~1 nm) of the electrode or separator, soft XAS measures at depths of 5 nm (TEY mode) and 100 nm (FY mode) (only TEY mode is recorded on the plot) and hard XAS measures deep into the bulk (~5 um). In the bulk, the pristine cathode shows a peak at the same energy as the Mn peak associated with Mn_2O_3. The peak energy of Mn in the cathode increases to a final energy of 6549.2 eV at the end of charge. The first-cycle charge capacity is affected by side reactions like oxygen loss and decomposition of Li_2O or Li_2CO_3 that do not involve Mn redox. At the end of discharge on the fifth cycle, the peak energy of Mn is lower than it was in the pristine cathode, indicating over-reduction of Mn during cycling. Mn in the separator remains at a very similar valence state throughout the charging and discharging process, and is close to that found for the cathode. The largest difference is after 5 cycles, where the separator is much more oxidized than the cathode.

The trends for both cathode and separator at the surface, based on Mn L-edge soft XAS, are different from those in the bulk. Mn soft XAS access direct dipole transitions into the hybridized 2p-3d transitions in high resolution, providing rich multiplet spectra that have a lot of contrast between different chemical states, which allow us to extract Mn valence with relatively high precision, which we have labelled for each measurement in the figure. The Mn at the surface of the pristine cathode is at a valence state of +2.8, which is slightly more reduced compared to the trivalent Mn in the bulk, but as the material is charged to 4.2 V the Mn near the surface becomes oxidized to the tetravalent state (+3.8).[26] Upon further charging Mn is reduced to a final valence state of +2.0. Both the hard and soft XAS indicate that the cathode after 5 cycles, stopped in the discharged state, has a final valence lower than its initial value of ~3. Mn at the surface of the separator in the cell charged to 4.4 V (there was no Mn detected in the separator from the cell charged to 4.2 V) is at its lowest valence state of +2.0. This indicates that cell charge to between 4.2 V to 4.4 V is a key step driving Mn dissolution, as it is only after this point where there is a high enough concentration of Mn on the separator to detect it. Moreover, Mn^{3+} disproportionates into Mn^{4+} and Mn^{2+} in

the presence of proton-containing species.[25] The existence of Mn^{4+} at the surface of the charged cathode and Mn^{2+} on the separator is consistent with past literature. When Mn initially migrates to the separator, it is in the form Mn^{2+}, which then becomes oxidized as the cell is charged to 4.6 and then 4.8 V. At the end of discharge after 5 cycles, the Mn on the separator surface is again at a +2.0 valence state, while, in the bulk of the separator, Mn has a peak energy more similar to that of trivalent Mn. This is in contrast to the cathode for which the bulk of the particle is also reduced along with the surface, although to a smaller degree. This indicates that there are surface reactions occurring with the Mn on the separator that do not penetrate into the bulk.

XPS on the very surface (~1 nm) of the cathode and separator may be influenced by interactions between Mn and surface organic material. Indeed, Mn at the surface of the cathode and separator shows only very small changes in binding energy during both charging and discharging, always remaining at similar energies as the signal from MnO_2 of 642.5 eV, while there are large differences between the O1s and C1s spectra taken at those same states of charge. While somewhat speculative, it is possible that Mn^{3+} disproportionates at the anode into 2+ and 4+ states. Due to the solubility of divalent Mn, it is likely washed away during processing of the cell components, which leaves primarily insoluble tetravalent Mn at the few-angstroms depth as measured by XPS. At high voltages, there is a competing effect between oxygen release and Mn^{2+} dissolution, which leaves a surface with a mixture of oxygen containing species as well as primarily Mn^{4+}. The presence of Mn^{2+} as measured by sXAS indicates that it is capable of remaining despite similar washing procedures if Mn^{2+} ions have penetrated sufficiently deep into the cathode and separator. Additionally, the relatively small changes in Mn binding energy (that is, oxidation state) indicate that once Mn^{4+} has formed at the surface, tetravalent Mn is relatively difficult to re-reduce, and tetravalent Mn therefore becomes a passivating layer.

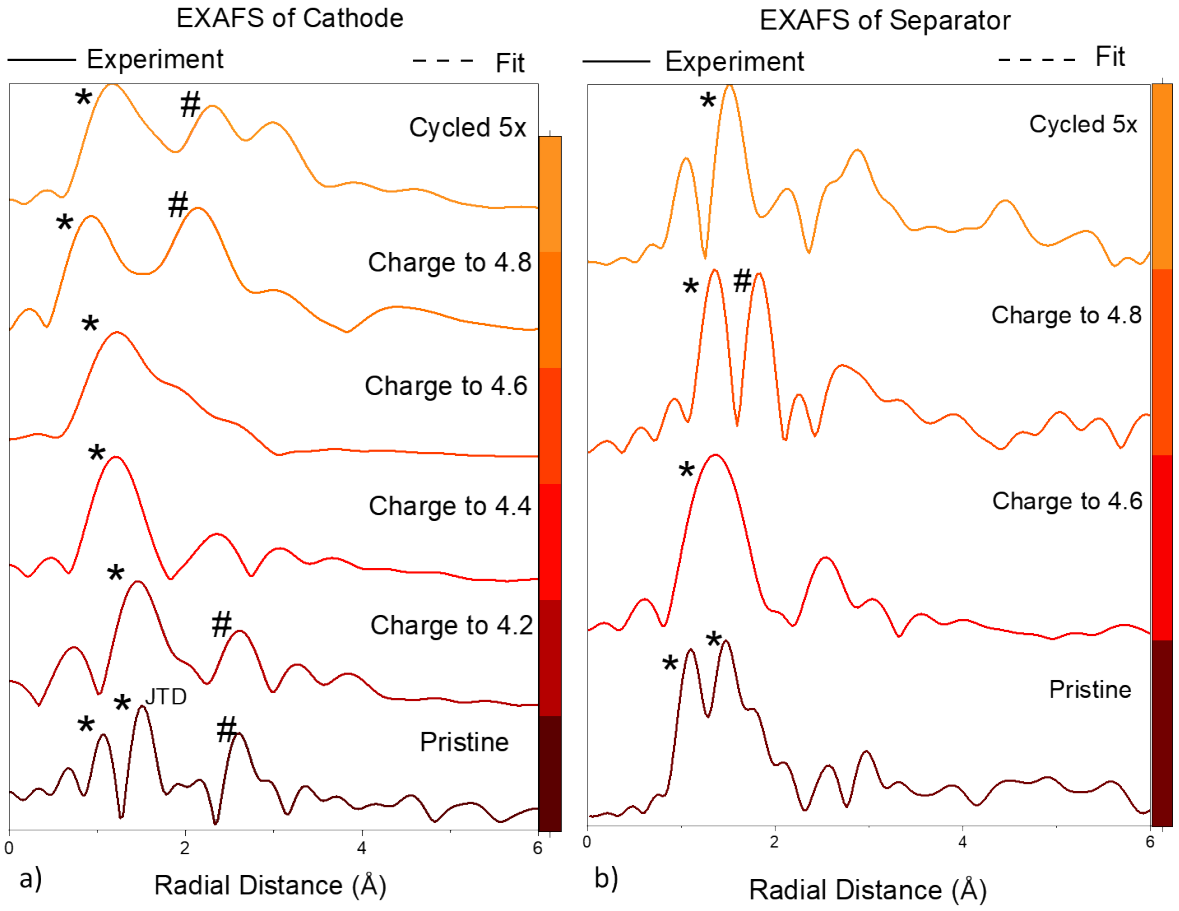

Figure 7. Phase-uncorrected FT EXAFS spectra obtained from k³-weighted χ(k) data in the range 0 – 11 A^{-1} obtained on cathodes a) and separators b) taken from cells charged or cycled to the indicated limits. These distances are not phase shift corrected and estimated to be 0.5 Å shorter than the reported bond lengths.[32] Asterisks (*) indicate Mn-O interactions, hash marks (#) indicate Mn-Mn interactions.[33,34]

Figure 7 shows phase-uncorrected Fourier Transformed EXAFS spectra from cathodes and separators recovered from cells charged or cycled to the indicated voltages (similar states of charge used in Figures 2-6). Though fitting was attempted, due to the complexity of the system and the insufficient statistics, we limit our discussion to the qualitative information in the data. The Mn in the pristine cathode shows clear evidence of Jahn Teller distortion (JTD),[24] with two peaks that can be assigned to Mn-O bonds, one at 1.5 Å[32] and the other at ultrashort length of 1.1 Å (uncorrected, the corrected lengths would be

approximately 1.6 Å and 2.0 Å). The specific phenomenon of JTD being present in a cathode material, and this additionally resulting in unusually short bond lengths, was observed by Whittingham et al.[24] with the cathode material Li_xMnPO_4. Upon delithiation of that material, Mn^{2+} oxidized to Mn^{3+}, and the single Mn-O peak measured by Mn K-edge EXAFS split into two with approximate uncorrected radial distances of 1.1 and 1.8 Å. In general, across charging for LMO, both the pristine material's XRD and FT EXAFS show very broad peaks, indicative of a highly disordered structure and implying a variety of possible nearest neighbors for Mn. Upon charging to 4.2 V, the two Mn-O features merges into a broader feature indicating that there is an increase in disorder and significantly reduced prevalence of J-T distortion. From 4.2 V to 4.8 V, the Mn-O peak is progressively shifted to lower radial distance, consistent with lattice contraction during delithiation. Additionally, we observe a broadening of the Mn-O peak with increasing charge potentials indicating that the local environment becomes even more disordered, due to the presence of lithium vacancies and other factors.

Previous literature reports by Manceau et al.[33] on naturally-occurring minerals indicate that Mn-Mn distances in compounds containing MnO_6 octahedra have a corrected distance of approximately 2.8-3.0 Å (across two edge-sharing octahedra) and approximately 3.4-3.6 Å (across three edge sharing octahedra).[33–35] Upon charging, we observe that the Mn-Mn peak (marked with hash sign) is at lower radial values and broadened, indicating a lattice contraction and increased broadening during delithiation, similar to the Mn-O peak. At 4.8V, we observe an increase in the Mn-Mn peak relative to the Mn-O peak. Moreover, the sample cycled 5x, which is stopped in the discharged state, appears to regain similar distances as for the pristine material, but with much broader features, and with notable absence of J-T splitting, and stronger presence of the second Mn-Mn peak. Lee et al. measured EXAFS of a surface-modified spinel $LiMn_2O_4$ cathode material, which provides a point of reference for how EXAFS of a spinel local environment should appear.[35] In the spectrum of LMO charged to 4.8 V, the peak due to Mn-Mn interaction is more intense than the one due to Mn-O. Similarly, the Mn-Mn peak in the spinel is more intense than the Mn-O peak, at all points throughout the charging and discharging. In contrast, the EXAFS of non-spinel

manganese oxides measured by Manceau et al., as well as manganese oxide colloids as measured by Suib et al., show much weaker Mn-Mn peaks.[33,34] Lee et al. measured Mn-O bond distances of 1.91 Å and Mn-Mn interaction lengths of 2.85-2.91 Å. In comparison, the LMO cathode charged to 4.8 V has (corrected) Mn-O radial distances of 1.5 Å and Mn-Mn radial distances of 2.6 Å. This indicates spinel-like character, but is clearly different from a fully crystalline spinel.

Hard XAS indicates that the Mn in the separator remains in an approximately 3+ state on average throughout the charging process, though Mn in the separator is at a higher oxidation state than the cathode at the end of discharge after five cycles. On the pristine separator, the local environment of Mn is much different from the local environment in the cathode. We disregard any peaks above 3 Å as simply background signal. However, the EXAFS results at lower distances show that there are significant changes in the coordination environment of the Mn in the separator as the cell is cycled, and that this occurs despite the average oxidation state of the manganese in the separator remaining relatively constant. Combined with the XPS and hard and soft XAS observations, this suggests that there are numerous electrochemical and chemical processes involved in the dissolution and subsequent reactions of Mn from the cathode.

Conclusions

Spectroscopic analysis at different depths of components taken from charged, discharged, and cycled cells containing LMO reveal the complexity of Mn dissolution. Dissolution at room temperature is mainly observed when cells are charged above ~4.2 - 4.4 V and occurs concomitantly with oxygen release, decomposition of adventitious Li_2CO_3 or Li_2O, and structural rearrangement in the cathode material. While the oxidation state of bulk Mn in the separator, which arises from dissolution from the cathode, closely follows the oxidation state of the Mn in the cathode as the cell is charged, Mn in the separator is not reduced past Mn^{3+} after cycling several times to the discharged state, unlike the Mn in the cathode. Surface sensitive techniques (XAS and XPS) reveal a more dynamic picture for Mn in the separator as the cell is charged, indicating that Mn in the separator does not necessarily follow the same redox pathway as Mn in the cathode. Mn at the very surface of the separator, as revealed by XPS experiments, appears to be more

oxidized than Mn at the very surface of the cathode. However, Mn at the very surface remains in approximately the same valence state throughout charging and discharging, which could indicate a disproportionation mechanism during which Mn^{2+} is washed away and Mn^{4+} remains as a stabilizing layer at high voltages. Qualitative EXAFS analysis shows evidence of irreversible structural changes of the cathode material upon cell charge, consistent with increased disorder. Thus, dissolution of Mn in cells containing LMO initiates a complex set of phenomena, which may contribute to capacity fading.

Data Availability

The data that support the findings in this study are available upon request. Additional data can be found in the Supplimentary Information.

Author Contributions

M. T. carried out the synthesis, all of the electrochemical fabrication and characterization, the hard XAS characterization including EXAFS qualitative analysis, and analysis of all X-ray data (hard XAS, soft XAS, XPS) under supervision of M. D. and W. T.; D. N. performed soft XAS measurements and provided expertise in their analysis. C. D. performed XPS measurements under the supervision of J. U. Both M. T. and M. D. wrote the original draft, and all authors reviewed and provided their edits.

Acknowledgments

This work was supported by the Assistant Secretary for Energy, Efficiency and Renewable Energy, Office of Vehicle Technologies of the U.S. Department of Energy under Contract No. DE-AC02-05CH11231. Work at the Molecular Foundry of Lawrence Berkeley National Lab (LBNL), supported by the Office of Science, Office of Basic Energy Sciences of the U.S. Department of Energy under Contract No. DE-AC02-05CH11231. We would like to acknowledge the use of the Stanford Synchrotron Radiation Lightsource, SLAC National Accelerator Laboratory, that is supported by the U.S. Department of Energy, Office of Science, Office of Basic Energy Sciences under Contract No. DE-AC02-76SF00515.

1 R. J. Clément, Z. Lun and G. Ceder, *Energy Environ Sci*, 2020, **13**, 345–373.

2 J. Lee, A. Urban, X. Li, D. Su, G. Hautier and G. Ceder, *Science (1979)*, 2014, **343**, 519–522.

3 M. Freire, N. V. Kosova, C. Jordy, D. Chateigner, O. I. Lebedev, A. Maignan and V. Pralong, *Nature Materials*, 2015, **15**, 173–177.

4 Y. Yue, N. Li, Y. Ha, M. J. Crafton, B. D. McCloskey, W. Yang, W. Tong, Y. Yue, N. Li, B. D. McCloskey, W. Tong, Y. Ha, W. Yang and M. J. Crafton, *Adv Funct Mater*, 2021, **31**, 2008696.

5 J. Ahn, R. Giovine, V. C. Wu, K. P. Koirala, C. Wang, R. J. Clément and G. Chen, *Adv Energy Mater*, 2023, **13**, 2300221.

6 S. Ahmed, S. E. Trask, D. W. Dees, P. A. Nelson, W. Lu, A. R. Dunlop, B. J. Polzin and A. N. Jansen, *J Power Sources*, 2018, **403**, 56–65.

7 Y. Yue, Y. Ha, R. Giovine, R. Clément, W. Yang and W. Tong, *Chemistry of Materials*, 2022, **34**, 1524–1532.

8 J. Ahn, D. Chen and G. Chen, *Adv Energy Mater*, 2020, **10**, 2001671.

9 C. Zhan, T. Wu, J. Lu and K. Amine, *Energy Environ Sci*, 2018, **11**, 243–257.

10 J. C. Hunter, *J Solid State Chem*, 1981, **39**, 142–147.

11 J. R. Dahn, E. W. Fuller, M. Obrovac and U. von Sacken, *Solid State Ion*, 1994, **69**, 265–270.

12 Z. Zhang, D. Fouchard and J. R. Rea, *J Power Sources*, 1998, **70**, 16–20.

13 A. Blyr, A. Du Pasquier, G. Amatucci and J. M. Tarascon, *Ionics (Kiel)*, 1997, **3**, 321–331.

14 G. Amatucci, A. Du Pasquier, A. Blyr, T. Zheng and J. M. Tarascon, *Electrochim Acta*, 1999, **45**, 255–271.

15 S. K. Martha, J. Grinblat, O. Haik, E. Zinigrad, T. Drezen, J. H. Miners, I. Exnar, A. Kay, B. Markovsky and D. Aurbach, *Angewandte Chemie International Edition*, 2009, **48**, 8559–8563.

16 W. Choi and A. Manthiram, *J Electrochem Soc*, 2006, **153**, A1760.

17 C. Zhan, J. Lu, A. Jeremy Kropf, T. Wu, A. N. Jansen, Y. K. Sun, X. Qiu and K. Amine, *Nature Communications*, 2013, **4**, 1–8.

18 C. S. Johnson, N. Li, C. Lefief, J. T. Vaughey and M. M. Thackeray, *Chemistry of Materials*, 2008, **20**, 6095–6106.

19 D. Mohanty, J. Li, S. C. Nagpure, D. L. Wood and C. Daniel, *MRS Energy & Sustainability*, 2015, **2**, E15.

20 F. Wu, W. Li, L. Chen, Y. Su, L. Bao, W. Bao, Z. Yang, J. Wang, Y. Lu and S. Chen, *Energy Storage Mater*, 2020, **28**, 383–392.

21 Y. Li, Z. Li, C. Chen, K. Yang, B. Cao, S. Xu, N. Yang, W. Zhao, H. Chen, M. Zhang and F. Pan, *Journal of Energy Chemistry*, 2021, **61**, 368–385.

22 J. Alvarado, C. Wei, D. Nordlund, T. Kroll, D. Sokaras, Y. Tian, Y. Liu and M. M. Doeff, *Materials Today*, 2020, **35**, 87–98.

23 C. Tian, D. Nordlund, H. L. Xin, Y. Xu, Y. Liu, D. Sokaras, F. Lin and M. M. Doeff, *J Electrochem Soc*, 2018, **165**, A696.

24 L. F. J. Piper, N. F. Quackenbush, S. Sallis, D. O. Scanlon, G. W. Watson, K. W. Nam, X. Q. Yang, K. E. Smith, F. Omenya, N. A. Chernova and M. S. Whittingham, *Journal of Physical Chemistry C*, 2013, **117**, 10383–10396.

25 H. Yaghoobnejad Asl and A. Manthiram, *J Am Chem Soc*, 2020, **142**, 21122–21130.

26 W. Yin, J. Alvarado, E. A. Kedzie, B. D. McCloskey, C. Dun, J. J. Urban, Z. Zhuo, W. Yang and M. M. Doeff, *J Mater Chem A Mater*, 2023, **11**, 23048–23061.

27 J. Xiao, N. Adelstein, Y. Bi, W. Bian, J. Cabana, C. L. Cobb, Y. Cui, S. J. Dillon, M. M. Doeff, S. M. Islam, K. Leung, M. Li, F. Lin, J. Liu, H. Luo, A. C. Marschilok, Y. S. Meng, Y. Qi, R. Sahore, K. G. Sprenger, R. C. Tenent, M. F. Toney, W. Tong, L. F. Wan, C. Wang, S. E. Weitzner, B. Wu and Y. Xi, *Nat Energy*. In preparation.

28 K. H. Nam, Z. Wang, J. Luo, C. Huang, M. F. Millares, A. Pace, L. Wang, S. T. King, L. Ma, S. Ehrlich, J. Bai, E. S. Takeuchi, A. C. Marschilok, S. Yan, K. J. Takeuchi and M. M. Doeff, *Chemistry of Materials*, 2024, **36**, 4481–4494.

29 A. Manceau, M. A. Marcus and S. Grangeon, *American Mineralogist*, 2012, **97**, 816–827.

30 F. Frati, M. O. J. Y. Hunault and F. M. F. De Groot, *Chem Rev*, 2020, **120**, 4056–4110.

31 M. C. Biesinger, B. P. Payne, A. P. Grosvenor, L. W. M. Lau, A. R. Gerson and R. S. C. Smart, *Appl Surf Sci*, 2011, **257**, 2717–2730.

32 B. Ravel and M. Newville, ATHENA, ARTEMIS, HEPHAESTUS: Data Analysis for X-Ray Absorption Spectroscopy Using IFEFFIT. *urn:issn:0909-0495*, 2005, **12**, 537–541.

33 Structural chemistry of Mn, Fe, Co, and Ni in manganese hydrous oxides: Part II. Information from EXAFS spectroscopy and electron and X-ray diffraction | American Mineralogist | GeoScienceWorld, https://pubs.geoscienceworld.org/msa/ammin/article/77/11-12/1144/42624/Structural-chemistry-of-Mn-Fe-Co-and-Ni-in, (accessed 21 July 2024).

34 T. Ressler, S. L. Brock, J. Wong and S. L. Suib, *Journal of Physical Chemistry B*, 1999, **103**, 6407–6420.

35 H. W. Chan, J. G. Duh and J. F. Lee, *Electrochem commun*, 2006, **8**, 1731–1736.